Chapter 3
EMC Oxidation Under High-Temperature Aging

A. Inamdar, P. Gromala, A. Prisacaru, A. Kabakchiev, Y. Yang, and B. Han

1 Thermal Aging of Epoxy Molding Compound

Epoxy molding compounds (EMC) are commonly used for housing the semiconductor chip and other internal circuitry of electronic packages. EMC protects electronic components and systems from various environmental conditions such as mechanical shock, chemical loads, heat, and moisture [1]. EMC is a composite material consisting of epoxy resin as the matrix, silica as the filler material, hardeners, and other additives [2]. The cross-linking reaction between epoxy resin and hardeners forms the thermosetting polymer.

A typical EMC contains very high content of silica filler, which helps in attaining desired thermomechanical properties. Hardeners contribute to the heat resistance and storage stability. Additives such as cure-promoter and flame-retardants provide increased reaction between epoxy and hardener and lower risk of flammability, respectively. The constituent materials of EMC contribute to its high adhesion strength, low shrinkage, excellent chemical resistance, and heat resistance [3]. The ability of EMC to be molded, its mechanical and chemical properties, and a relatively low cost compared to traditional ceramic packaging make it a better alternative as an encapsulating material. In the automotive industry, EMC is often used to protect not only single integrated-circuit (IC) packages but also entire electronic control units (ECU). Compared to the consumer electronics, automotive electronics

A. Inamdar (✉)
Delft University of Technology, Delft, The Netherlands
e-mail: A.S.Inamdar-1@tudelft.nl

P. Gromala · A. Prisacaru · A. Kabakchiev
Robert Bosch GmbH, Automotive Electronics, Reutlingen, Germany

Y. Yang · B. Han
University of Maryland, College Park, MD, USA

W. D. van Driel, M. Yazdan Mehr (eds.), *Reliability of Organic Compounds in Microelectronics and Optoelectronics*,
https://doi.org/10.1007/978-3-030-81576-9_3

is exposed to harsher environments such as moisture and temperature variation, which cause aging of EMC.

Aging can be defined as the long-term, irreversible changes that occur in a material due to its exposure to ambient conditions. The changes can be in the structure, composition, and morphology of the material [4]. In general, aging may result from a combination of mechanical loading and chemical changes. In case of an electronic package, aging refers to the changes occurring in its constituent materials during its operation-lifetime. Figure 3.1 shows a schematic diagram of a typical electronic package of the type quad flat no-leads (QFN). Among all of its components, the one most exposed to the atmosphere is the EMC. Therefore, the most important aging effect is usually the oxidation of EMC through the contact with atmospheric oxygen [4]. This type of aging is governed by the exposure to elevated temperatures, and hence it is referred as thermal aging of EMC.

The operating temperature around the automotive electronics located near a combustion engine or transmission can be as high as 150 °C [5]. Such exposure to high temperatures causes oxidation of EMC. This can significantly change its mechanical properties [6–8] and thus can affect the reliability of electronic components. Yet, only limited information can be found in the literature, and it is the motivation of the present study. This study focuses on the following key aspects of EMC oxidation –

- Experimental study of the time and temperature dependent growth of EMC oxidation layer, followed by developing an activation-energy-based mathematical model;
- Characterization of the thermomechanical properties of fully oxidized EMC specimens using standard experimental tests;
- Moiré interferometry-based comparison of the thermomechanical behavior of a thermally aged and pristine molded package during a temperature cycle;
- Finite element simulation-based solder-fatigue analysis of thermally aged molded package to determine its effect on solder joint reliability.

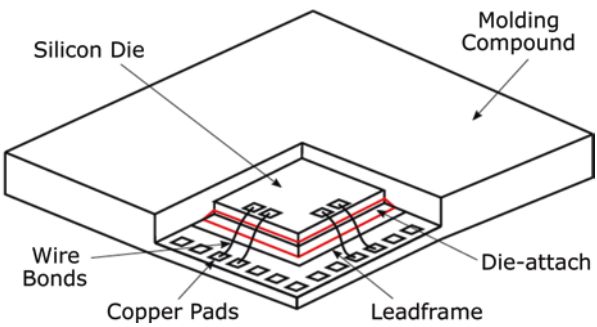

Fig. 3.1 Construction of a typical QFN package

2 Characterization of Oxidation Growth During Thermal Aging

EMC oxidation is a diffusion-based process, and thus the oxidation rate is time and temperature-dependent [9]. For complete characterization, the oxidation growth in EMC is measured as a function of time at various temperatures. The results are discussed to provide an insight into the oxidation process. The experimental data are utilized to develop an empirical model for oxidation growth.

2.1 Measurement of Oxidation Layer

EMC oxidation is time and temperature-dependent. It has been established that the oxidation layer grows with the increase in the ambient temperature, as well as the time-duration of its exposure to EMC [10]. Based on this qualitative information, a design of experiments was developed for quantifying the time-temperature dependency of the oxidation growth. A total of 24 specimens of EMC with a rectangular cross section (10 mm × 4 mm) were prepared for the test. Batches of eight specimens were subjected to three different high-temperature storage (HTS) conditions at 170 °C, 200 °C, and 230 °C, respectively. A single specimen was removed from each batch at 2, 4, 8, 24, 100, 500, 1000, and 1500 hours, and the thickness of the oxidation layer was measured.

After being removed from the HTS chamber, the specimen was sectioned and polished. Thickness measurements were performed using a fluorescence microscope equipped with ultraviolet illumination [11]. It is worth mentioning that an initial attempt was made using a digital microscope, but it was difficult to identify the oxide layer boundary clearly from the microscope images. Figure 3.2 shows representative fluorescence microscopy images, obtained from specimens aged for 1000 h at 170 °C, 200 °C, and 230 °C, respectively.

Under the fluorescence microscope, the pristine EMC was seen as green, while the oxide layer as light to dark brown. During aging at 230 °C, the oxide layer becomes dark brown, which is clearly distinguishable from pristine EMC. However, the specimens kept at lower temperatures show a prominent color gradient from brown to green, indicating the gradual transition from oxide layer to pristine EMC. In such cases, the gradient was closely observed, and the boundary was defined at the region where the brown portion of gradient ends and the green region begins.

For each specimen, 9 independent measurements of oxidation thickness were made and averaged to minimize the uncertainties associated with the boundary detection. A typical standard deviation was 1.1 μm, which established some guideline of thickness measurement accuracy.

The results are shown in Fig. 3.3. It is clear that the oxidation growth rate and thus the total thickness of the oxidized layer increases as the aging temperature

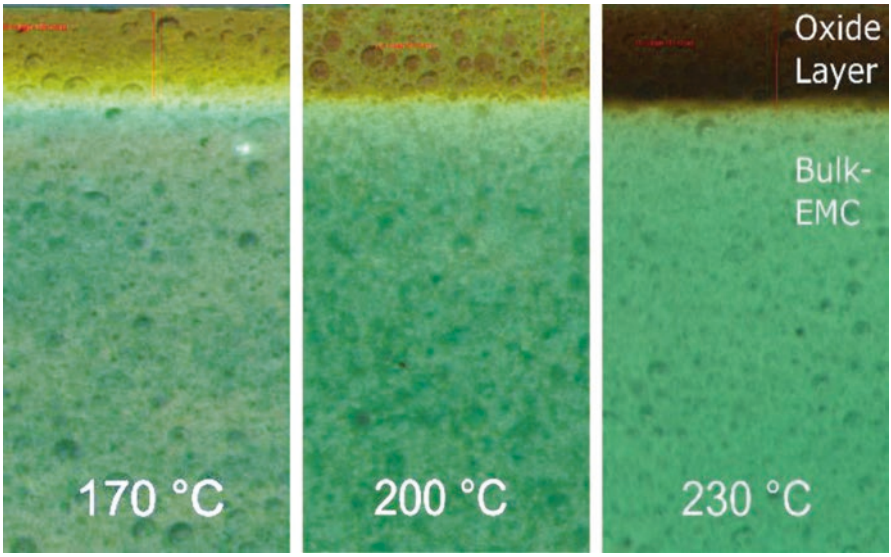

Fig. 3.2 Representative fluorescence microscope images obtained after 1000 h of thermal aging

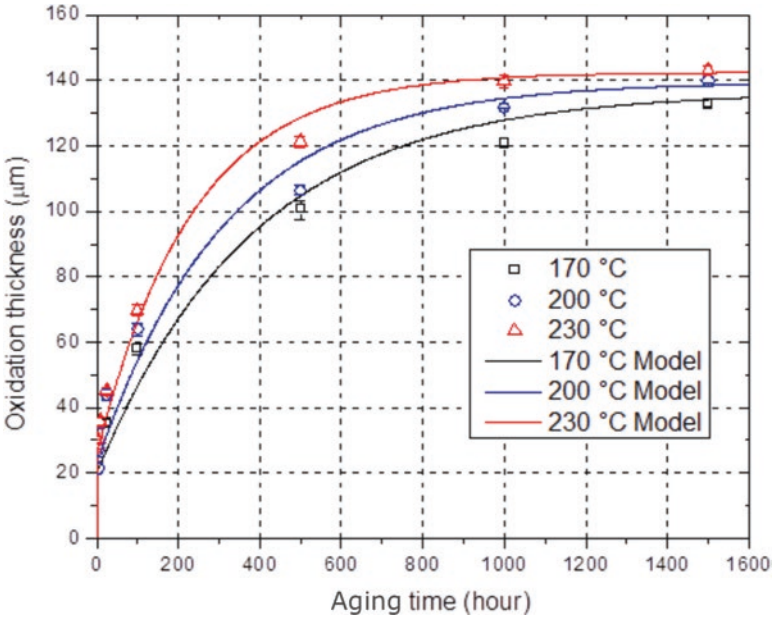

Fig. 3.3 Oxidation layer thickness as a function of aging time

increases. The thicknesses of the oxidized layer after 1500 h of aging are 133.0, 140.0, and 143.3 μm for the aging temperatures of 170 °C, 200 °C, and 230 °C, respectively.

It is important to note that the oxidized layer thickness increased rapidly during the first 30 h of aging. The thicknesses of the oxidized layer only after 24 h of aging were 35.5, 43.7, and 45.4 μm for 170 °C, 200 °C, and 230 °C, respectively. This is nearly 30% of the thickness of the oxidized layer after 1500 h.

2.2 Behavior of Oxidation Growth

Oxidation of EMC results from a combination of two processes – diffusion of oxygen and reaction of oxygen with EMC [8, 9]. Atmospheric oxygen diffuses into the porous network of EMC through its exposed surfaces. The diffused oxygen reacts with the matrix resin in EMC to form an oxide compound. As a result, a layer of oxidized EMC is formed along the exposed surface of the encapsulant. Both processes (i.e., diffusion and reaction) occur simultaneously, and the slower of these two determines the effective rate of oxidation.

When the reaction is slower than the diffusion, oxygen can diffuse into EMC beyond the oxide layer. As a result, the oxidation layer does not have a distinct separation from the pristine EMC, which is seen clearly in Fig. 3.2 in the fluorescence microscope image obtained at 170 °C. For the same reason, the diffused but unreacted oxygen could be found into the bulk of EMC [10]. On the other hand, when the reaction is faster than the diffusion, the diffused oxygen is consumed rapidly by the reaction. Furthermore, the oxidized layer hinders the diffusion, and thus the oxygen cannot penetrate beyond the oxide layer. One possible reason for this is the smaller diffusivity of the oxidized molding compound [12]. As a result, a more distinct oxide layer boundary can be observed. This can be seen clearly in Fig. 3.2 in the fluorescence microscope image obtained at 230 °C.

This can also be used to explain the rapid initial growth of the oxidized layer observed at all three aging temperatures. For a short period of time after the pristine EMC is placed inside the aging chamber, oxygen in the air diffuses freely into the pristine EMC, and is consumed simultaneously to produce the oxidized layer. As mentioned earlier, the oxidized layer slows down the oxygen diffusion process, which subsequently stabilizes the oxidation growth rate.

2.3 Empirical Model for Oxidation Growth

The measurements of oxidation layer thickness clearly show a trend of rapid initial growth, especially within the first 30 h of thermal aging. In addition, the growth rates decrease significantly after 500 h of storage. An empirical model, which can reproduce the aforementioned features, is proposed to predict the oxidation

thickness at different values of temperature and aging time. The proposed model can be expressed as:

$$h(t) = A(T) + B\left(1 - e^{-C(T)t}\right) \tag{3.1}$$

$$A(T) = a_1 T + a_2 \tag{3.2}$$

$$C(T) = C_0\, e^{-\left(\frac{E_C}{RT}\right)} \tag{3.3}$$

Equation (3.1) defines the oxidation thickness, h, as a function of time t. In the equation, $A(T)$ is a temperature-dependent constant that describes the rapid initial growth of oxidation, and it can be expressed as a linear function of T in Kevin (Eq. (3.2)), where a_1 and a_2 are constants. B is a temperature-independent constant, while the temperature-dependent constant $C(T)$ is defined by the Arrhenius relationship (Eq. (3.3)), where C_0 is a constant, E_C is the activation energy, and R is the ideal gas constant.

The parameters A, B, and C must be determined in order to completely define the empirical model. Model parameters were determined using the measured data and standard nonlinear regression techniques. The values are summarized in Table 3.1, and the oxidation growth curves predicted by the model are shown in Fig. 3.3.

3 Effect of EMC Oxidation on Thermomechanical Properties

Polymeric materials such as epoxy molding compounds typically show different mechanical behavior at different temperatures. There exists a certain characteristic temperature beyond which they transform from a glassy state to a rubbery state, and thus, they exhibit different thermomechanical properties. Figure 3.4 shows a typical variation of thermomechanical properties against temperature.

The transformation from glassy to rubbery state can be easily understood by the rapid fall in the value of elastic (storage) modulus with respect to increase in temperature, as indicated in Fig. 3.4a. Similarly, the coefficient of thermal expansions

Table 3.1 Parameters of empirical model

Parameter	Value
a_1 (μm/K)	0.1
a_2 (μm)	−24.3
B (μm)	116.58
C_0 (1/hour)	0.1662
E_C (J/mol)	1.5426×10^4

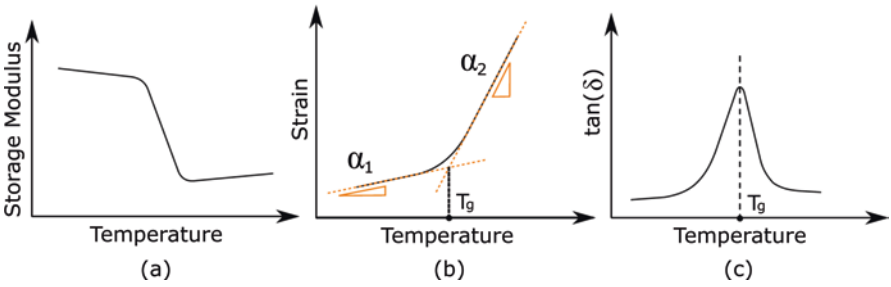

Fig. 3.4 Glass transition of polymeric materials – plots of (**a**) storage modulus, (**b**) thermal strain, and (**c**) tangent delta against temperature

(CTE), which is evaluated as the slope of thermal strain versus temperature plot as shown in Fig. 3.4b, also has 2 different values below and above the characteristic temperature. This phenomenon is known as glass transition, and the characteristic temperature is called as glass transition temperature T_g.

Three crucial thermomechanical properties of oxidized EMC are characterized – elastic (storage) modulus, E, glass transition temperature T_g, and coefficient of thermal expansion CTE. The standard experimental tests used for this characterization are – dynamic mechanical analysis (DMA) and thermomechanical analysis (TMA).

3.1 Study of Partially Oxidized EMC Specimens

Experimental study of the effect of thermal aging on thermomechanical properties of EMC can be found in the literature. In [10], EMC specimens were subjected to various sets of standard thermal aging processes, e.g., sold reflow, thermal cycling, high-temperature storage, etc. Similarly, in [12, 13], thermomechanical properties were characterized using EMC specimens, which were thermally aged (high-temperature storage) for different time duration.

Experimental characterization using these specimens shows anomalies. For example, instead of a typical single peak in the tan(δ) versus temperature plot (Fig. 3.4c), two local maxima were observed for the aged specimens. The second peak clearly indicates the presence of a second phase in the material, i.e., the oxide layer [13]. In other words, this suggests that the oxidation layer should also exhibit different thermomechanical behavior than the bulk of EMC.

It is important to note that these experimental tests were carried out on partially oxidized EMC specimens. In [10], purely analytical methods have been described for evaluating effective material properties of oxidized EMC on the basis of experimental data of the partially oxidized EMC specimens. In this study, fully oxidized specimens were prepared and tested to avoid any ambiguity in measured properties.

3.2 Preparation of Fully Oxidized EMC Specimens

Thin specimens (≈ 300 μm thickness) were fabricated by grinding molded parts (≈ 2 mm thickness) that were prepared for mechanical testing. The thin specimens are shown with the regular specimens in Fig. 3.5. The thin specimens were then stored at a constant temperature of 150 °C for 2000 h. Based on the data shown in Fig. 3.3, it was expected that complete oxidation occurred through the specimen, as oxidation occurred from both top and bottom surfaces of the specimen. This was later confirmed by observing the cross sections under the fluorescence microscope. The image of the cross section is shown in Fig. 3.6, where complete oxidation over the thickness is evident.

3.3 Experimental Characterization of Thermomechanical Properties

Thermomechanical properties of the fully oxidized EMC specimens are compared with those of the pristine EMC specimens.

3.3.1 Storage Modulus

The storage modulus was obtained using dynamic mechanical analysis (DMA) under three-point bending mode, which is illustrated schematically in Fig. 3.7. Storage modulus is proportional to the maximum elastic energy stored during one

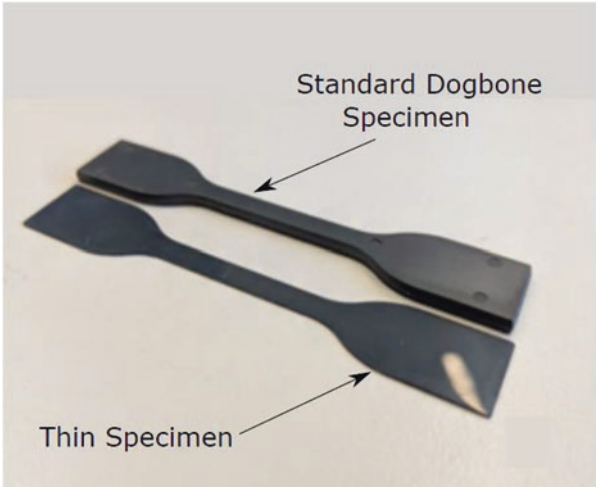

Fig. 3.5 Thin EMC specimens after grinding

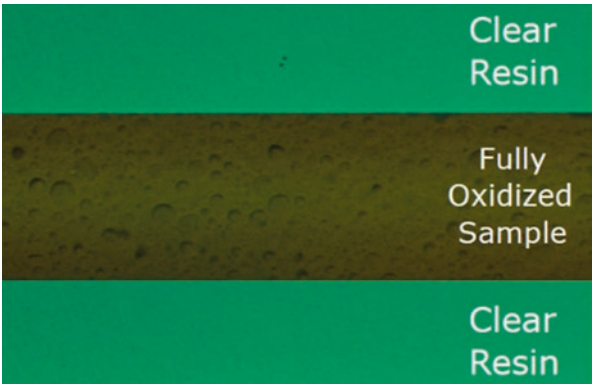

Fig. 3.6 Cross section of fully oxidized thin specimen

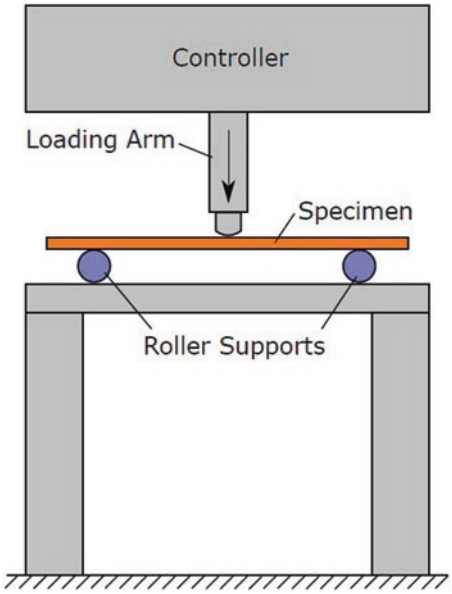

Fig. 3.7 Schematic diagram of DMA test in three-point bending mode

load period, and thus the plot of storage modulus versus temperature obtained from DMA is used for assessing the elastic properties of a material.

Figure 3.8 shows the temperature-dependent storage moduli of pristine and fully oxidized EMC specimens, obtained at a frequency of 10 Hz. The plot clearly indicates that the modulus of EMC increased significantly for the entire range of temperatures after oxidization. For example, the modulus of oxidized EMC at room temperature (20 °C) increased by nearly 20%. It is important to mention that the beginning of the transition zone of oxidized EMC is shifted by nearly 80 °C, and the transition zone of oxidized EMC is widened as well.

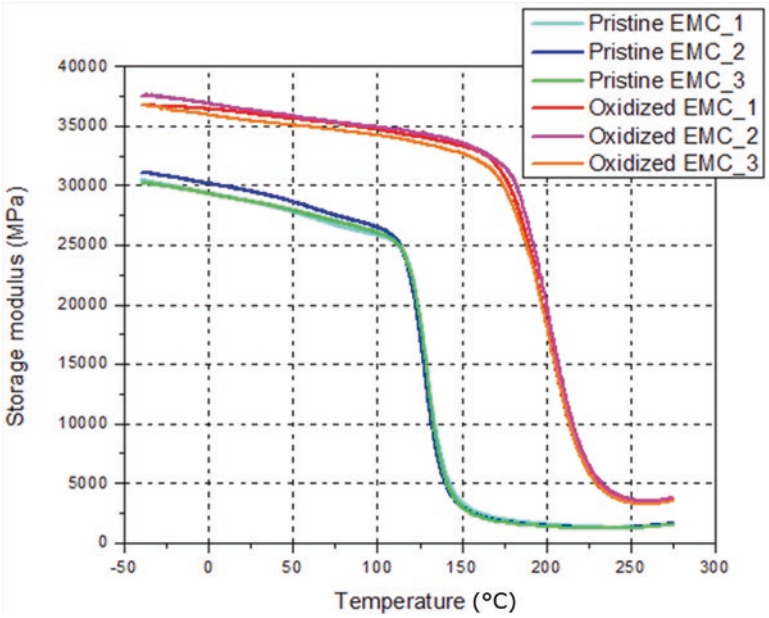

Fig. 3.8 Comparison of DMA results for pristine and oxidized EMC

3.3.2 Coefficient of Thermal Expansion

Coefficient of thermal expansion (CTE) can be measured routinely by Thermomechanical Analyzer (TMA). The specimens used for thermomechanical property characterizations are, however, too thin (≈ 300 μm) to be measured by TMA. A full-field displacement measurement technique called digital image correlation (DIC) was employed instead to measure the CTE of fully oxidized and pristine EMC specimens. The experimental setup of DIC is shown schematically in Fig. 3.9. An integrated heating plate provides an accurate temperature control, and two cameras record the images of a specimen surface. The procedure to measure CTE using the DIC technique is straightforward. Two images of a specimen are captured before and after temperature change, and then a DIC analysis proceeds with those images to determine thermally induced displacements [14], from which thermal strains, and thus CTE are determined.

Figure 3.10 shows a representative deformation field obtained at 120 °C, where the horizontal lines in black color are the paths used for strain calculations. Thermal strains obtained from DIC tests are shown in Fig. 3.11. The glass transition temperature, T_g, and the CTEs below and above T_g (α_1 and α_2, respectively) were determined from the strains, and the results are summarized in Table 3.2.

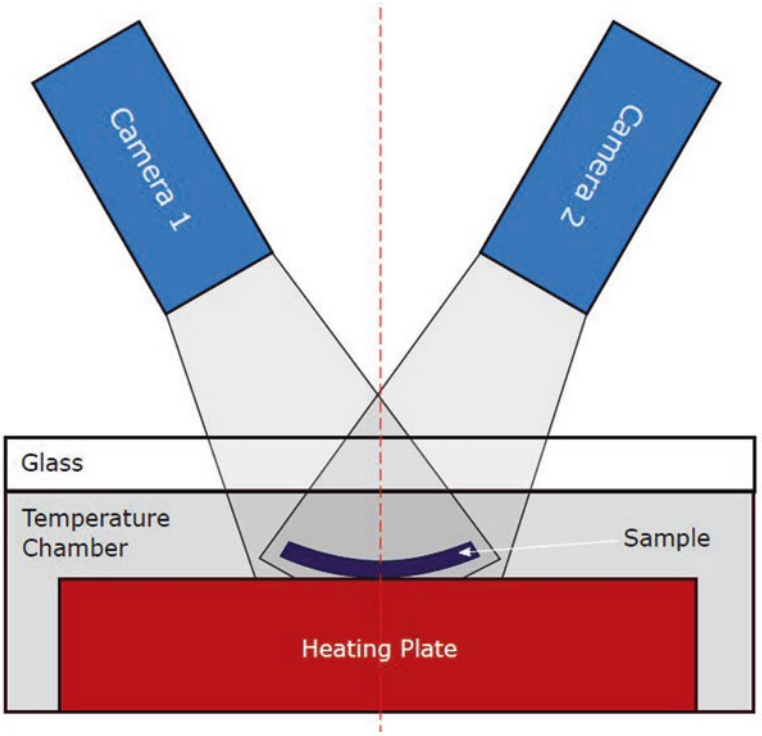

Fig. 3.9 Schematic illustration of the DIC setup

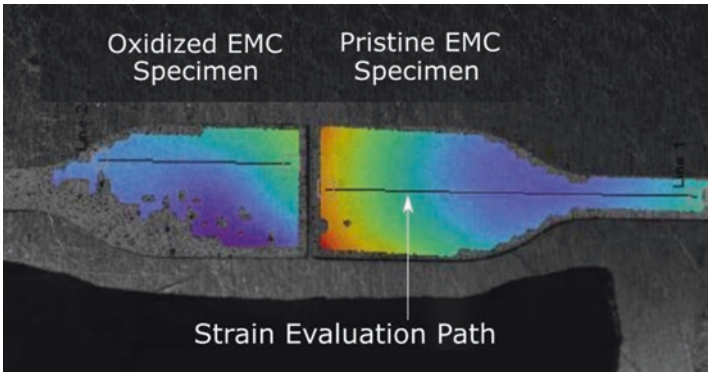

Fig. 3.10 Evaluation of thermal strain at 120 °C along a path using DIC software

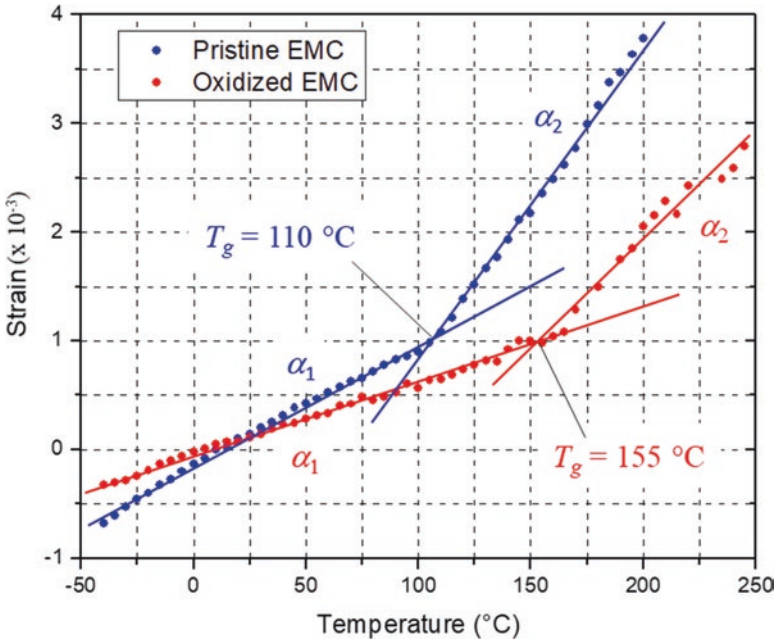

Fig. 3.11 Comparison of DIC results for pristine and fully oxidized EMC

Table 3.2 CTE values for pristine and fully oxidized EMC

	T_g (°C)	α_1 (ppm/°C)	α_2 (ppm/°C)
Pristine EMC	110	11.4	30.3
Oxidized EMC	155	6.5	20.2

As expected from the DMA results, oxidized EMC shows a significantly higher value of T_g (an increase of 45 °C). The CTE values of oxidized EMC are much lower than the corresponding values of pristine EMC for the entire range of temperatures; the CTEs of oxidized EMC have become 57% and 66% of those of pristine EMC below and above T_g, respectively. It is worth noting that the largest CTE difference (23 ppm/°C) occurs in the temperature range between $T_g^{pristine}$ and $T_g^{oxidized}$.

These results highlight that the thermomechanical properties of oxidized EMC are significantly different from those of pristine EMC, and the properties of oxidized EMC must be considered when reliability of devices subject to a long period of high temperature operating conditions is to be assessed. A next section is devoted to an investigation of the effect of the oxidation layer on the thermomechanical behavior of a package.

4 Effect of EMC Oxidation on Thermomechanical Behavior of Package

An electronic package typically consists of multiple layers of different materials, molding compound being the outermost one. Due to the differences in the thermomechanical properties of different materials involved in the multi-layered structure of a package, temperature changes can lead to mismatch in the thermal expansion of individual components. This causes warping of the entire structure and stresses are generated within as well as along the interfaces of different components. These stresses can lead to different failure mechanisms, and thus their quantification is an important aspect of reliability assessment of an electronic system.

Thermal aging of an electronic package causes oxidation of EMC along its exposed surfaces. Due to the significantly different thermomechanical properties of oxidized EMC, the behavior of the entire electronic package can also be affected significantly. The effect of oxidation layer on the thermomechanical behavior of an actual package is studied by an optical technique called moiré interferometry.

4.1 Preparation of Thermally Aged Package Specimens

Quad flat no-leads (QFN) packages were used for testing. The dimension of the package is 12 mm × 12 mm × 0.85 mm. The internal structure of the QFN package is schematically shown in Fig. 3.12a. For an automobile with a combustion engine, the operating temperature of electronic components located near an engine can be as high as 150 °C [5]. In real world usage, a consumer car is used for about 10 h a week [15, 16]. Thus, in just 4 years, the components would be subjected to a high operating temperature for more than 2000 h. Therefore, the QFN package specimens were thermally aged at 150 °C for 2000 h.

After thermal aging process, cross sections of a few specimens were prepared using the same procedure described before for the measurement of oxidation layer thickness. Figure 3.12b shows the cross-section observed under the microscope. The presence of a thick oxide layer as well as a gradient from fully oxidized to pristine EMC is clearly visible. The measured thickness is ≈ 150 μm, which matches reasonably well the value calculated using the empirical model (132 μm).

Two thermally aged specimens as well as two pristine QFN packages were analyzed by moiré interferometry. The packages were cut in half along one of the planes of symmetry, and ground flat for specimen grating replication.

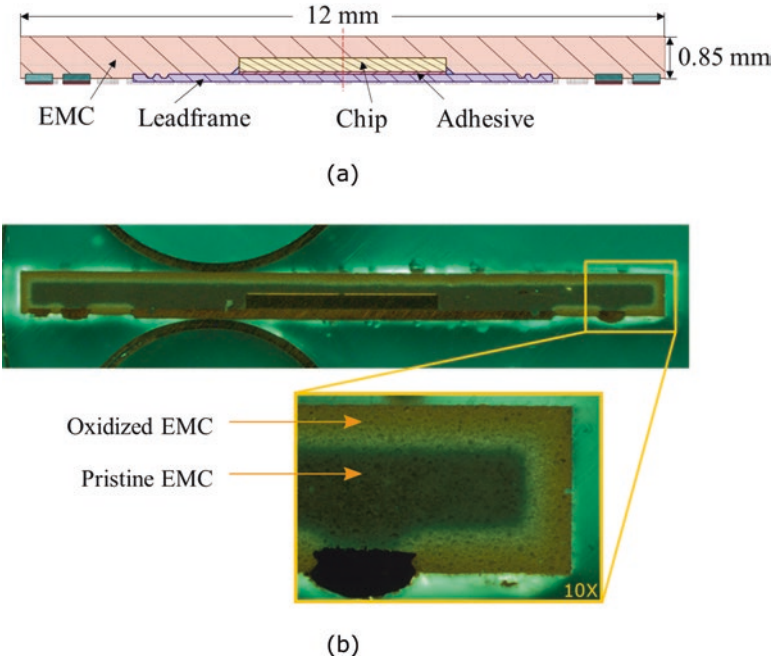

Fig. 3.12 Cross section of QFN package specimen – (**a**) internal structure (**b**) oxidation layer due to thermal aging at 150 °C for 2000 h

4.2 Experimental Analysis Using Moiré Interferometry

Real-time moiré interferometry was employed to investigate the effect of the oxidized layer on the package deformations. Moiré interferometry is a full-field optical technique to measure the in-plane deformations with high sensitivity [17], and it has been used widely for electronic packaging design and reliability assessment [18]. The outputs are the contour maps of in-plane displacements, which are related to the fringe orders by:

$$U(x,y) = \frac{1}{f} N_x(x,y) V(x,y) = \frac{1}{f} N_y(x,y) \tag{3.4}$$

where N is the fringe order and f is the frequency of the virtual reference grating. In routine practice, a virtual reference grating with a frequency of 2400 lines/mm is used, which provides a contour interval of 417 nm per fringe order.

The optical/mechanical configuration used in the study is illustrated in Fig. 3.13. It consists of (1) a portable engineering moiré interferometer that provides two sets of virtual reference gratings and (2) a conduction chamber built on a

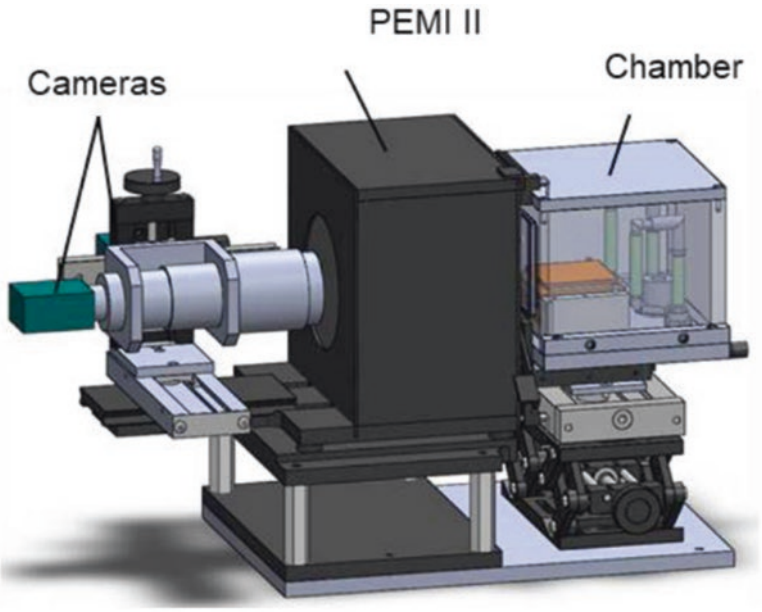

Fig. 3.13 Schematic illustration of the optical/mechanical configuration for moiré interferometry

high-performance thermo-electric cooler that provides accurate temperature control. The thermal conduction chamber is mounted on an *x*-*y*-*z* translation stage, which allows positioning as well as focusing the specimen. More details of the system can be found in Ref. [19].

The specimen gratings with a frequency of 1200 lines/mm were replicated on the cross sections at room temperature (20 °C). The details about the grating and replication procedures used in this study can be found in [17, 20]. The packages with the gratings were then heated to 85 °C and 150 °C, and the thermal deformations were documented by the moiré system. It is to be noted that the first temperature (85 °C) is below the T_g values of both pristine and oxidized EMCs, while the second one (150 °C) lies between the T_g values of the pristine and oxidized EMC.

The *U* and *V* fringe patterns of the right half of the package, representing the in-plane displacements in the *x* and *y* directions, respectively, are shown in Fig. 3.14, where the contour interval is 417 nm per fringe. The displacements were evaluated along the path defined in the top inset of Fig. 3.15 to investigate the effect of oxidized EMC on the package behavior. The results are shown in Fig. 3.15a, b for 85 °C and 150 °C, respectively.

As expected, the results at 85 °C show similar behaviors. At 150 °C, however, two packages exhibit radically different behaviors. The *U* displacement of the pristine package is much larger than that of the oxidized package, while the *V* displacement of the pristine package is significantly smaller than that of the oxidized package. The larger *U* displacement of the pristine package at 150 °C is attributed to the fact that the testing temperature is higher than T_g of the pristine EMC but

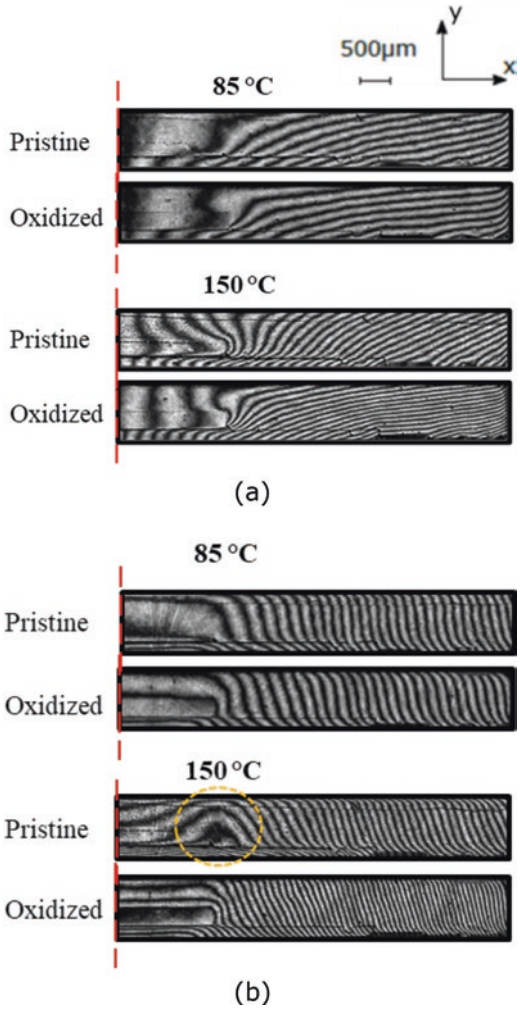

Fig. 3.14 (**a**) U-field and (**b**) V-field displacements of the right half of the package, obtained at 85 °C and 150 °C, where the contour interval is 417 nm per fringe

below T_g of the oxidized EMC. The relatively low CTE of the oxidized EMC also contributed to the large difference.

The most peculiar difference was seen in the *V* displacements at 150 °C. The *V* or bending displacements are caused mainly by the CTE mismatch between the EMC and the leadframe. The CTE of the leadframe is 16.2 ppm/°C, which is much larger than α_1 (the CTE below T_g) of both pristine and oxidized EMCs. As a result, heating from room to 85 °C produced upward bending (∪). The pristine EMC passes T_g (110 °C) during the second stage of heating to 150 °C. The CTE above T_g, α_2, is 30.3 ppm/°C, which is larger than the leadframe CTE. Consequently, the second stage of heating produced downward bending (∩), and thus the net bending displacement of the pristine package was reduced at 150 °C (from 11 μm to 9 μm). The

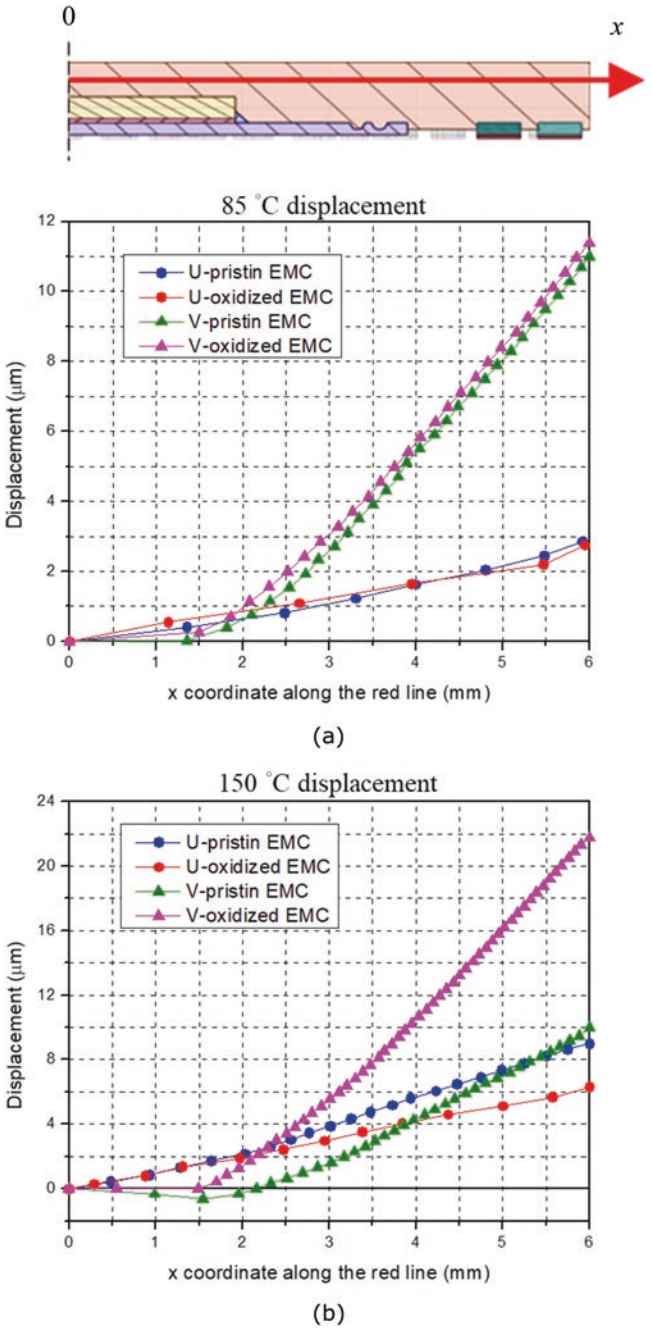

Fig. 3.15 U- and V-displacement at (**a**) 85 °C and (**b**) 150 °C along the red line

unusual bending displacement near the chip, marked by a dotted circle in Fig. 3.14b, was caused by this complex loading condition.

In the oxidized package, the package behavior was controlled by the thick oxide layer surrounding the package, as shown Fig. 3.12b due to its high modulus. Although a large amount of pristine EMC was still present inside, the large modulus of the oxidized EMC did not allow the pristine EMC to deform freely. In addition, the oxidized EMC remained below T_g (155 °C) during the second stage of heating, i.e., the CTE remained as α_1. The net result was that the bending displacements were proportional to ΔT. The bending displacement at 85 °C was 11 μm, which was caused by ΔT of 65 °C (= 85–20) and the bending displacement at 150 °C was 22 μm, which was caused by ΔT of 130 °C (= 150–20). This stiffer behavior must be considered when long-term board-level reliability is to be assessed.

5 Effect of EMC Oxidation on Reliability of Electronic Components

Electronic components have a wide range of failure modes, viz. packaging failure, contact failure, PCB failure, and semiconductor failure. Causes of failure range from a sudden change in temperature, excess current or voltage, mechanical shock, stress or impact, etc., to the fatigue caused by prolonged exposure of these parameters. Statistics show that 70% of the failures are related to packaging and assembly, and the primary reason behind them is the solder joint failure [21]. Moreover, about 45% of the failures are caused by the exposure of ambient thermal conditions [22]. Thus the failure of solder joint due to the temperature variation is one of the most important modes of failure.

5.1 Fatigue Failure of Solder Joints

Solder fatigue is the mechanical degradation of solder joint due to its deformation under cyclic loading. As a result of repeated temperature fluctuations, mechanical vibrations, or mechanical loads, fatigue failure occurs often at stress levels below the yield stress of the solder material. For this study, the effect of temperature cycles is considered.

An electronic package can experience various temperature cycles during its multi-step fabrication and assembly process as well as during its operation lifetime. Temperature variation causes warping of the package due to the CTE-mismatch among its constituent components. This leads to cyclic stresses within the package as well as within the solder joints. Standard temperature cycles from −40 °C and 150 °C were considered for the reliability assessment under solder-fatigue. There are several models for analyzing thermal fatigue failure of solder joints. They can be

classified as – strain-based, stress-based, and energy-based models [22]. For this study, a strain-based model was considered.

EMC oxidation results into a much stiffer behavior of the QFN package under a temperature cycle. This change in behavior can significantly affect the solder fatigue. A finite-element simulation-based analysis was carried out to study the effect of oxidation layer on the solder joint reliability. A calibrated model of the QFN package including its geometry and material behavior was utilized. The procedure of modeling and calibration is discussed in this section.

5.2 Modelling of Package Geometry

An accurate solid model of the QFN package was prepared based on extensive measurements carried out using X-ray imaging and digital microscope. Cross sections of the package-PCB assembly at different locations were prepared. Most important dimensions such as chip dimensions, die-attach meniscus, EMC height, copper-pads dimensions, solder standoff height, etc., were measured carefully. Important features such as the skew shape of the solder joints, resulting from an offset between copper pads on the QFN package and on the PCB, were precisely replicated in the model. An average value of solder stand-off height was determined for the model by fitting a plane to the spatial plot of the solder-height data.

Subsequently, the solid model was further divided into multiple sub-components based on the requirements of stress-evaluation and finite-element mesh. In the ANSYS Workbench environment, a finite-element mesh was generated using a combination of 20-node homogeneous (hexahedral) structural solid and 10-node tetrahedral structural solid 3D elements.

5.3 Modeling of Material Properties

5.3.1 QFN Package

The QFN package consists of following materials – silicon, adhesive, copper, and molding compound. Two well-known materials – copper and silicon – were modeled as temperature-dependent linear elastic isotropic and orthotropic materials, respectively. Material behaviors of EMC and adhesive materials are highly viscoelastic. Based on the complexity of the simulation-based analysis and the available experimental data, an equivalent linear elastic model was proposed for each material. Experimental results discussed in the Sect. 3 of this chapter were utilized for preparing models of the pristine and oxidized EMC. The equivalent material models were calibrated using the thermomechanical behavior of QFN packages, in order to reproduce the effective viscoelastic behavior of these materials.

5.3.2 Calibration Using Moiré Interferometry

Experimental results from real-time moiré interferometry were utilized for the calibration. The models were modified over several iterations of finite-element simulations. Due to the symmetry, a quarter model of the QFN package with appropriate constraints replicating the experimental conditions was utilized. Calibration was carried out at 85 °C, 125 °C, and 150 °C in the same order. Figure 3.16 shows the simulation results of *U*-field and *V*-field displacement at 85 °C using the calibrated models. Further calibration was carried out at 125 °C and subsequently at 150 °C. The simulation results at 150 °C using the finalized model are shown in Fig. 3.17. Note that two different sets of models for adhesive, pristine-EMC, and oxidized-EMC were created for the case of pristine-package and aged-package, respectively.

During calibration, the elastic modulus of adhesive was significantly reduced (from 0.17 GPa to 0.01 GPa) after its T_g in both sets of models for replicating an effective viscoelastic relaxation. Similarly, the elastic modulus of pristine-EMC was significantly reduced to 0.15 GPa after its $T_{g,}$ but only in the case of pristine-package. This allows reproducing the W-shaped deformation curve, as indicated in Fig. 3.17.

In contrast, for the case of aged-package, the much stiffer outer layer of the oxidized-EMC did not allow the pristine-EMC in the bulk to relax. Therefore, the corresponding model of pristine-EMC was left unchanged. Material models of the oxidized-EMC for both sets did not require any modification.

5.3.3 Solder and PCB

Solder joint was modeled as a viscoplastic material, and accumulated plastic strains after each thermal cycle were evaluated. Solder alloys can have different compositions, which can lead to different microstructures (i.e., variations in phases, grain size, etc.) [23]. For simplicity, the effect of microstructures was not considered. Instead, the bulk behavior of solder joint was calculated by a rate-dependent inelastic model with kinematic hardening.

Lastly, considering the construction of the PCB, it was modeled as a single substrate material with equivalent linear elastic orthotropic material properties. All material models were assigned to their respective components in ANSYS environment using an APDL script.

5.4 Solder Fatigue Analysis

5.4.1 Simulation Settings

Finite-element simulation was carried out using a quarter geometry of the package-PCB assembly with appropriate symmetry boundary conditions. Figure 3.18 shows the quarter geometry model of the QFN package. The oxidation layer within the

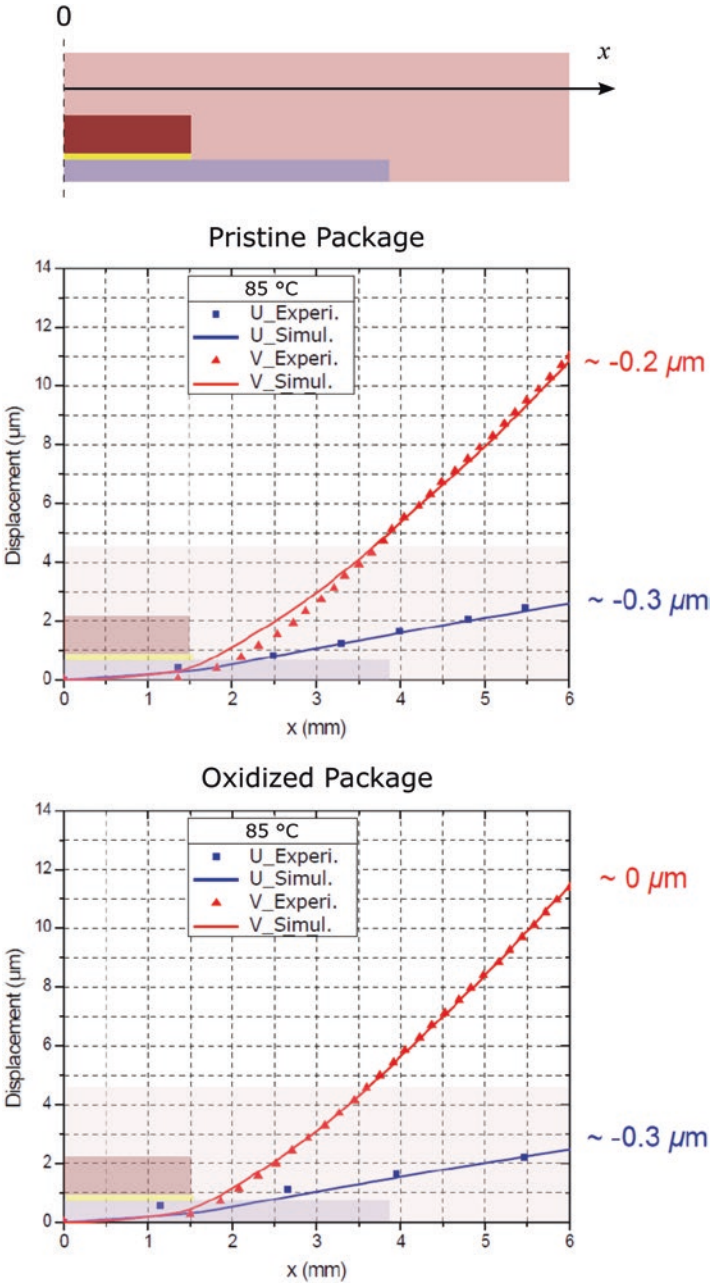

Fig. 3.16 Calibration of model at 85 °C using moiré interferometry simulation

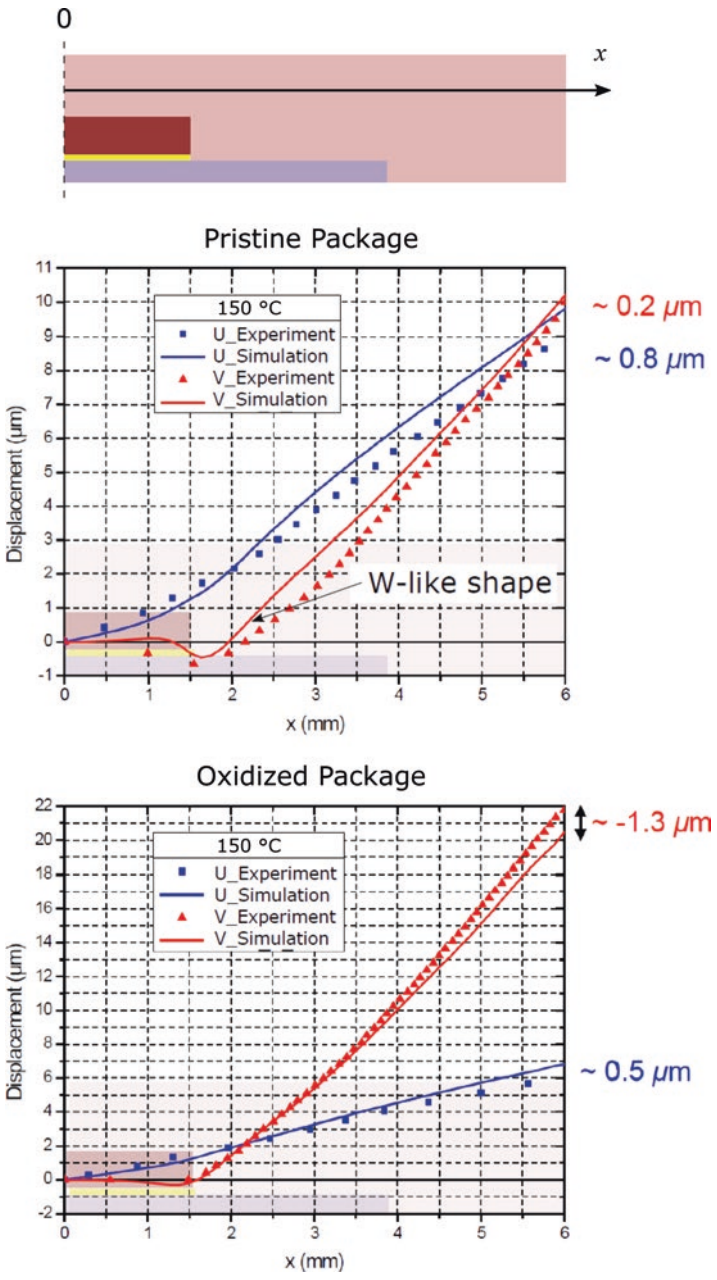

Fig. 3.17 Simulation results at 150 °C using finalized model

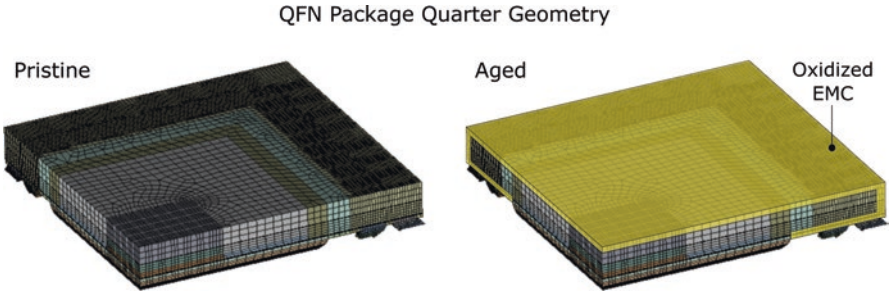

Fig. 3.18 Oxidation layer within the finite-element model of QFN package

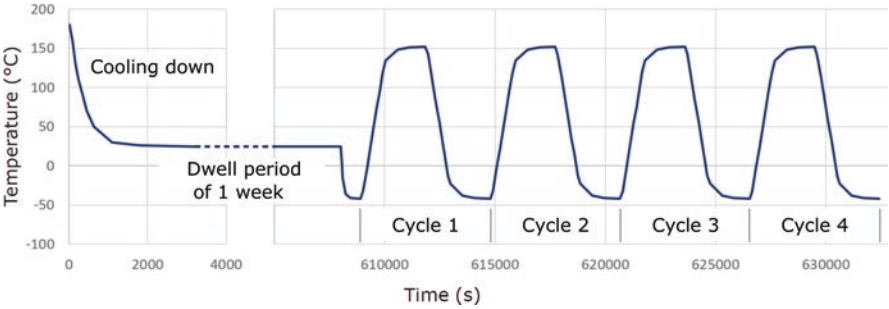

Fig. 3.19 Thermal condition for solder fatigue analysis

thermally aged QFN package was represented with a separate (150 μm thick) layer of elements within the EMC.

Figure 3.19 shows thermal loading conditions used in the analysis. It consists of three parts – (1) cooling down from 180 °C to 25 °C after the reflow soldering process, (2) dwell period of 1 week corresponding to the actual storage of components, (3) thermal cycles (−40 °C to 150 °C) used for standard reliability tests. It is important to note that the first two parts are necessary to replicate the real-world conditions, which introduce residual stresses within the solder joints and stress relaxation due to the prolonged storage, respectively.

5.4.2 Simulation Results

Fatigue failure of the solder material is caused by crack initiation and propagation, which is quantified as the accumulated fatigue damage, in this case – the accumulated plastic strain (APS) over several thermal cycles. A damage parameter for a

solder joint is evaluated based on the APS of all of its elements. It is a volume-based weighted average of the APS, and thus represents a single value for the entire solder joint (SJ).

For this study, a damage parameter "DP20" was utilized, which is based on the finite elements with highest value of APS and constituting 20% of the SJ volume. Figure 3.20a shows an example of a solder joint, highlighting the elements selected for the calculation of DP20. Among all solder joints, indicated with numbers in Fig. 3.20b, SJ-9 showed the highest DP20 values in each temperature cycle, and thus it was monitored closely.

Convergence of the strain energy density accumulated during each cycle was studied in Ref. [24]. It was observed that regardless of the type of solder (with or without lead), at least 3 thermal cycles are required for the convergence of the averaged strain energy density. Therefore, more than 4 cycles were considered for this study. Figure 3.21 shows the DP20 value for SJ-9 after each thermal cycle.

Values of DP20 for both pristine and aged packages converged well after sixth cycle. Up to 8 cycles were studied to confirm this, and the values corresponding to eighth cycle were utilized for a further analysis. Damage parameter of SJ-9 in the pristine-package starts with a much higher value, but converges to a lower value than the aged-package. The comparison of converged values shows that the aged-package has about 0.06% more plastic strain accumulated per cycle than the pristine-package. Preliminary estimation of the fatigue life was carried out using the Coffin-Manson relation and the DP20 values of SJ-9 after eighth thermal cycle.

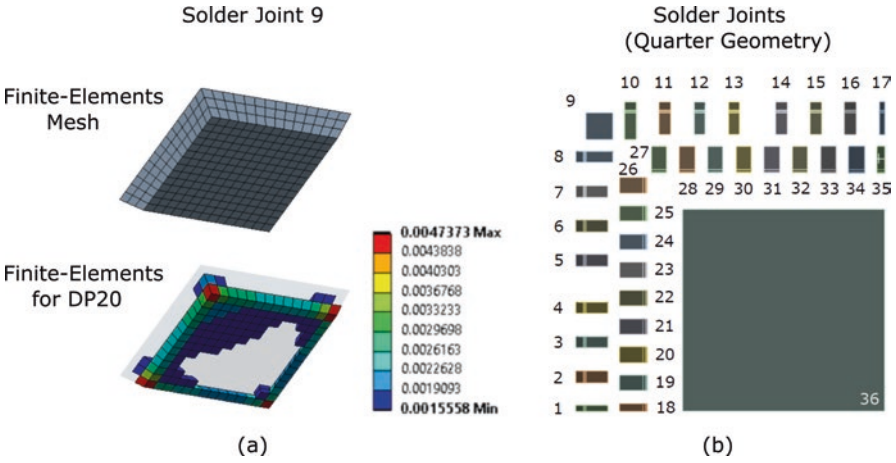

Fig. 3.20 Finite-element simulation – (**a**) evaluation of damage parameter for SJ-9 and (**b**) layout of solder joints for the quarter geometry of QFN package

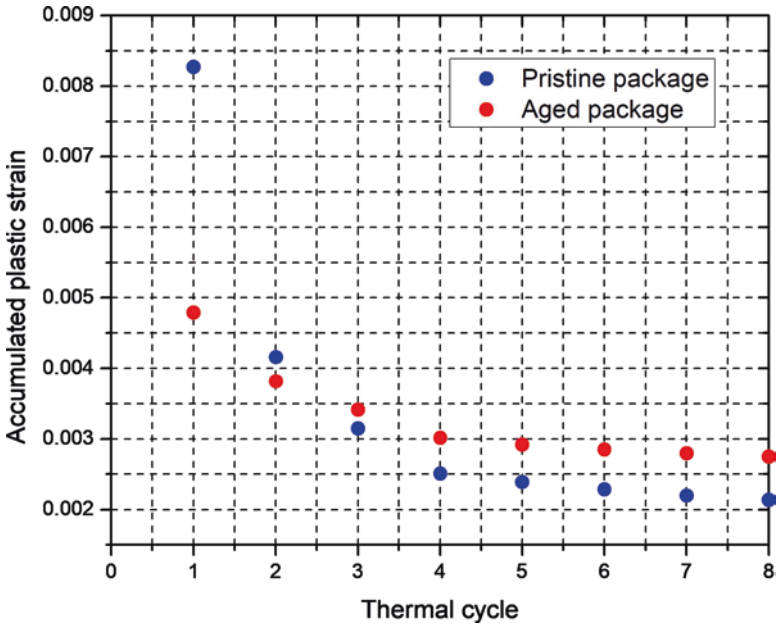

Fig. 3.21 Convergence of accumulated plastic strain values for SJ-9

Coffin-Manson model describes the relationship between the fatigue-lifetime of a material undergoing cyclic loading, and it is expressed as:

$$\left(\Delta\varepsilon^{pl}/2\right) = \varepsilon_f \left(2N\right)^C \tag{3.5}$$

where $\Delta\varepsilon^{pl}$ is accumulated plastic strain in one cycle; N is the number of cycles before failure (fatigue-lifetime); ε_f is fatigue ductility coefficient, which roughly corresponds to the true elongation at breaking point in a quasi-static tensile test; and C indicates fatigue ductility, which has value in the range $[-0.7, -0.5]$ for ductile materials [25]. For the sake of the first order comparison, the value of C is assumed to be -0.6 for the solder material. Thus, the ratio of the fatigue-lifetime of solder joints between the pristine and aged packages can be given as:

$$\frac{N_{aged}}{N_{pristine}} = \left(\frac{\Delta\varepsilon^{pl}_{aged}}{\Delta\varepsilon^{pl}_{pristine}}\right)^{1/C} \approx \frac{2}{3} \tag{3.6}$$

Due to the same solder material used in pristine and aged package, corresponding ε_f values are the same. Substituting $\Delta\varepsilon^{pl}_{aged}$ and $\Delta\varepsilon^{pl}_{pristine}$ with the corresponding values of DP20 of SJ-9 after 8th thermal cycle, the ratio is approximately $\left(2/3\right)$.

The result implies that the oxidation layer would cause 33% reduction in the lifetime of the solder joints, which is significant.

6 Conclusion

Thermal aging of epoxy molding compound (EMC) leads to its oxidation. The process of oxidation and its effects on the material and package-level thermomechanical behavior as well as on the solder joint reliability was studied. The growth of an oxidation layer was first determined experimentally by subjecting EMC specimens to various aging temperatures. The results clearly showed the temperature-dependent rate increase. It was also observed that the thickness of the oxidation layer increased rapidly at the early stage of aging ($\approx$ 30 h). An activation energy-based empirical model was proposed for predicting oxidation layer thickness as a function of aging time and temperature, and the model constants were determined using the experimental results.

In the second task, thin EMC specimens were prepared to produce fully-oxidized test specimens, and they were tested to obtain three crucial thermomechanical properties of oxidized EMC. The results clearly showed significant changes in properties after oxidization, specifically (1) an increase of the elastic modulus, (2) a decrease of CTE, and (3) an increase of T_g. As the third task, the effect of oxidation layer on the thermomechanical behavior of an actual package encapsulated by EMC was investigated by an optical technique called moiré interferometry. A thermally aged package exhibited a much stiffer behavior under a thermal cycle, compared with a pristine package. This behavior change should be considered for accurate reliability assessment.

Lastly, the effect of EMC oxidation on thermal fatigue of the solder joints was studied using finite-element analyses. A set of calibrated models for the behavior of a pristine and an aged QFN package were utilized. The ratio of the number of cycles for fatigue-failure between aged and pristine QFN was evaluated based on the converged accumulated plastic strain using the Coffin-Manson model. The results showed that the oxidation layer could cause as much as 33% reduction in the solder joint life.

Acknowledgments A part of the work has been performed in the project ArchitectECA2030 under grant agreement No. 877539. The project is co-funded by grants from Germany, Netherlands, Czech Republic, Austria, Norway and Electronic Component Systems for European Leadership Joint Undertaking (ECSEL JU).

A part of the work was funded by the Federal Government of Germany, Framework Program for Research and Innovation 2016-2020 Microelectronics – Innovation Drivers of Digitalization (Rahmenprogramm der Bundesregierung für Forschung und Innovation 2016-2020 Mikroelektronik aus Deutschland – Innovationstreiber der Digitalisierung) – Project smartSTAR (No. 16ES0965). This funding is gratefully appreciated.

References

1. K.M.B. Jansen, J. de Vreugd, L.J. Ernst, C. Bohm, Thermal aging of molding compounds, 11th International Conference on Electronic Packaging Technology & High Density Packaging 2010, (August 2010), pp. 778–780
2. E. Nguegang, J. Franz, A. Kretschmann, H. Sandmaier, Aging effects of epoxy moulding compound on the long-term stability of plastic package, 11th International Conference on Thermal Mechanical and Multiphysics Simulation and Experiments in Micro-Electronics and Micro-Systems EuroSimE 2010, (April 2010), pp. 1–6
3. M. Linec, B. Mušič, The Effects of Silica-Based Fillers on the Properties of Epoxy Molding Compounds. Materials **12**(11), 1811 (2019)
4. C.J.G. Plummer, Testing of Polymeric Materials, in *Comprehensive Materials Processing*, (Elsevier Publication, 2014), pp. 35–70
5. E.H. Amalu, N.N. Ekere, R.S. Bhatti, High temperature electronics: R&D challenges and trends in materials, packaging and interconnection technology, 2nd International Conference on Adaptive Science & Technology (ICAST), (December 2009), pp. 146–153,
6. J. de Vreugd, K.M.B. Jansen, L.J. Ernst, C. Bohm, R. Pufall, High temperature storage influence on molding compound properties, 11th International Conference on Thermal Mechanical and Multiphysics Simulation and Experiments in Micro-Electronics and Micro-Systems EuroSimE 2010, (April 2010), pp. 1–6
7. J. de Vreugd, A. Sanchez Monforte, K.M.B. Jansen, L.J. Ernst, C. Bohm et al., Effect of postcure and thermal aging on molding compound properties", 11th Electronics Packaging Technology Conference 2009, (December 2009), pp. 342–347
8. R. Li, D. Yang, P. Zhang, F. Niu, M. Cai, G. Zhang, Effects of high-temperature storage on the elasticity modulus of an epoxy molding compound. Materials **12**(4), 684 (2019)
9. A. Quintana, M.C. Celina, Overview of DLO modeling and approaches to predict heterogeneous oxidative polymer degradation. Polym. Degrad. Stab. **149**, 173–191 (2018)
10. E.N. Ngnetiwe, Experimental and Simulation-based Investigations on the Influence of Thermal Aging and Humidity on the Warpage of Molded Plastic Packages, PhD Thesis, Institute for Micro Integration, University of Stuttgart, (2013)
11. F. Rost, Fluorescence Microscopy, Applications, in *Encyclopedia of Spectroscopy and Spectrometry* (Third Edition, 2017), pp. 627–631
12. B. Zhang, M. Johlitz, A. Lion, L. Ernst, K.M.B. Jansen, D.K. Vu, L. Weiss, Aging of Epoxy Moulding Compound - Thermomechanical Properties during High Temperature Storage, 17th International Conference on Thermal, Mechanical and Multi-Physics Simulation and Experiments in Microelectronics and Microsystems (EuroSimE), (April 2016), pp. 1–6
13. J. de Vreugd, The Effect of Aging on Molding Compound Properties, PhD Thesis, Delft University of Technology (TU Delft), (2011)
14. B. Pan, K. Qian, H. Xie, A. Asundi, Two-dimensional digital image correlation for in-plane displacement and strain measurement: a review. Measurement Sci. Technol. **20**(6) (2009)
15. A. Stetzer, Americans Spend More Time Behind the Wheel, Despite Reduction in Daily Mobility, According to Ketchum's Daily Ride Index, Ketchum. Retrieved from https://www.prnewswire.com/news-releases/americans-spend-more-time-behind-the-wheel-despite-reduction-in-daily-mobility-according-to-ketchums-daily-ride-index-300863559.html, 06 June 2019
16. G. Pasaoglu, D. Fiorello, A. Martino, G. Scarcella, A. Alemanno, A. Zubaryeva, C. Thiel, Driving and Parking Patterns of European Car Drivers - a Mobility Survey, Scientific and Technical Research Reports, European Commission, Publications Office of the European Union, (2012)
17. D. Post, B. Han, P. Ifju, High Sensitivity Moire: Experimental Analysis for Mechanics and Materials, Mechanical Engineering Series, Springer, 1994. (Student edition, 1997)
18. B. Han, Thermal stresses in microelectronics subassemblies: quantitative characterization using photomechanics methods. J. Therm. Stress. **26**(6), 583–613 (2003)

19. B. Wu, B. Han, Advanced mechanical/optical configuration of real-time moire interferometry for thermal deformation analysis of fan-out wafer level package. IEEE Trans. Comp. Packaging Manuf. Technol. **8**(5) (2018)
20. B. Han, Recent advancements of moire and microscopic moire interferometry for thermal deformation analyses of microelectronics devices. Exp. Mech. **38**(4), 278–288 (1998)
21. R. Tilgner, Physics of failure for interconnect structures: An essay. Microsyst. Technol. **15**(1), 129–138 (2009)
22. X. Li, R. Sun, Y. Wang, A Review of Typical Thermal Fatigue Failure Models for Solder Joints of Electronic Components, IOP Conference Series: Materials Science and Engineering, Volume 242, 2017 and 3rd International Conference on Applied Materials and Manufacturing Technology (ICAMMT 2017) 23–25, (June 2017)
23. W. Engelmaier, *Solder Joints in Electronics: Design for Reliability* (Workshop Notes, Engelmaier Associates, Inc., 1999)
24. C. Han, B. Han, Board level reliability analysis of chip resistor assemblies under thermal cycling: A comparison study between SnPb and SnAgCu. J. Mech. Sci. Technol. **28**, 879–886 (2014)
25. M. Rocotta, Simple expressions to estimate the Manson-Coffin curves of ductile cast irons. Int. J. Fatigue **78**, 38–45 (2015)